Microchimica Acta (2023) 190:59
https://doi.org/10.1007/s00604-023-05635-z

ORIGINAL PAPER

Cu_2O@PdAg-quenched CdS@CeO_2 heterostructure electrochemiluminescence immunosensor for determination of prostate-specific antigen

Zhengxing Gong[1,2] · Xinrong Shao[1,2] · Jing Luo[1,2] · Xu Sun[1,2] · Hongmin Ma[1,2] · Dan Wu[1,2] · Dawei Fan[1,2] · Yuyang Li[1,2] · Qin Wei[1,2] · Huangxian Ju[1,2,3]

Received: 15 June 2022 / Accepted: 25 December 2022 / Published online: 19 January 2023

Abstract

Based on the resonance energy transfer between CdS@CeO_2 and Cu_2O@PdAg, a quenching immunosensor for sensitive detection of prostate specific antigen (PSA) was constructed. The CdS@CeO_2 heterostructure was obtained by in situ growth of CeO_2 particles on the surface of CdS nanorods, and stable cathodic ECL emission was achieved using $K_2S_2O_8$ as coreactant. Cu_2O@PdAg was composed of Cu_2O with tetradecahedral structure and bimetallic PdAg nanospheres and has a UV–V is absorption range between 600 and 800 nm. It overlaps with the ECL emission spectrum of CdS@CeO_2, realizing the effective quenching of the ECL signal, which provides feasibility for subsequent practical application. The immunosensor exhibited good linearity in the concentration range 10 fg·mL^{-1} ~ 100 ng·mL^{-1}, with a detection limit of 5.6 fg·mL^{-1}. In sample analysis, the recoveries were 99.8–101%, and the relative standard deviation (RSD) was 0.85–1.6% showing great potential and development value for the sensitive detection of prostate cancer.

Keywords Electrochemiluminescence · Immunosensor · Nanorods · CdS@CeO_2 · Cu_2O@PdAg · PSA · Resonance energy transfer

Introduction

Cancer is considered to be one of the deadliest diseases facing human beings, among which prostate cancer is one of the deadliest cancers in men. Early detection and treatment are the keys to defeating and curing cancer [1]. According to the American Cancer Society, prostate cancer can be diagnosed early by the biological level of prostate specific antigen (PSA) in the blood [2]. PSA is secreted by prostate epithelial cells and is present in prostate tissue and semen [3, 4]. PSA concentrations between 4 and 10 ng·mL^{-1} are considered suspicious, and patients need to be repeated or tested with an alternative confirmatory assay [5, 6]. In recent years, various immunoassays have been studied for the detection of PSA, such as enzyme-linked immunoassay [7], photoelectrochemical immunoassay [8], fluorescence immunoassay [9], capillary electrophoresis immunoassay [10], surface plasmon body resonance [11], and electrochemical immunoassay [12]. Electrochemiluminescence (ECL) combines optical sensitivity with electrochemical controllability and is a reliable means for biological detection [13, 14]. It has unique advantages such as high sensitivity, low background signal, high spatial resolution, strong operability, high throughput, wide response range, and simple instrumentation. Finding a reliable electrochemiluminescence material has become a hot spot and challenge in current research [15–17].

Zhengxing Gong and Xinrong Shao contributed equally to this work.

✉ Dawei Fan
jndxfandawei@126.com

[1] Collaborative Innovation Center for Green Chemical Manufacturing and Accurate Detection, School of Chemistry and Chemical Engineering, University of Jinan, Jinan 250022, People's Republic of China

[2] Key Laboratory of Interfacial Reaction & Sensing Analysis in Universities of Shandong, School of Chemistry and Chemical Engineering, University of Jinan, Jinan 250022, People's Republic of China

[3] State Key Laboratory of Analytical Chemistry for Life Science, School of Chemistry and Chemical Engineering, Nanjing University, Nanjing 210023, People's Republic of China

Furthermore, electrochemiluminescence-resonance energy transfer (ECL-RET) is an analytical strategy based on resonance energy transfer between efficient ECL emitters and energy acceptors with overlapping spectra [18, 19]. This analytical strategy is highly sensitive and can act as a kind of ECL signaling switch to manipulate signal quenching or amplification. Due to its high stability and large light absorption coefficient efficiency [20, 21], Cu_2O is widely used in photovoltaics, photocatalysis, and other fields and is also one of the commonly used quenchers in electrochemiluminescence sensors [18, 22]. The introduction of the second metal can effectively modify the electronic structure of Pd and produce a special synergistic effect with it, enhancing the conductivity and enriching the superficial active sites [23]. Therefore, small-sized PdAg bimetallic nanospheres were prepared by a one-pot method and loaded onto the Cu_2O surface with a regular tetrahedral structure with enhanced electrical conductivity and biocompatibility.

In addition, the biological activity of the antigen–antibody has a great influence on the performance of the immunosensor [24]. The $F(ab')_2$ fragment is the active part of the antibody that specifically binds to the antigen [25]. When only part of it participates in the immobilization process, the antibody activity will be significantly reduced. The development of small peptide ligands opens the way for targeted antibody immobilization on nanocarrier surfaces [26]. In particular, HWRGWVC heptapeptide (HGC) has been shown to be able to specifically bind to amino acids of antibody Fc fragments with high affinity and has the advantages of low cost, easy preparation, good stability, localization, and immobilization of antibodies in immunoassays outstanding advantages [27].

In summary, rod CdS was synthesized, and CeO_2 was loaded on its surface as the cathode near-infrared ECL emitter (energy donor), and Cu_2O@PdAg is used as the quencher (energy acceptor). Moreover, based on the resonance energy transfer between them, a quenching ECL immunosensor for sensitive detection of PSA was constructed and through a series of characterizations and tests, the successful construction of the sensor is verified. For the detection of PSA, the immunosensor exhibited good linearity and low detection limit in a wide detection range and demonstrated practical feasibility in sample detection.

Experimental section

All reagents and testing instruments can be viewed in the support information.

Synthesis of CdS@CeO_2 nanocomposites

The synthesis steps of CdS can be found in the supporting literature. Then 2 mmol of CdS prepared above and 1 mmol of $Ce(NO_3)_3{\cdot}6H_2O$ were weighed and dissolved in 20 mL of ultrapure water by ultrasonic, and then 20 mL of 6 M sodium hydroxide solution was added. After stirring evenly, it was transferred to the reaction kettle and reacted at 180 °C for 24 h. After centrifugation, the CdS@CeO_2 nanocomposites were obtained by washing with water and ethanol three times, respectively, and vacuum drying overnight. In order to connect the antibody, CdS@CeO_2 was aminated, and the CdS@CeO_2-NH_2 nanocomposite with amino groups was further obtained. The detailed steps are shown in the supporting information.

Preparation of Cu_2O@PdAg-HGC-Ab_2 bioconjugates

Three milligrams of the above synthesized Cu_2O@PdAg solid was dissolved in 1 mL of PBS (phosphate buffer saline, pH = 7.4). Then, 100 μL of HGC solution (10 μg·mL^{-1}), 1 mL of EDC (1-(3-dimethylaminopropyl)-3-ethylcarbodiimide hydrochloride) solution (4 mg·mL^{-1}), and 1 mL of NHS (N-hydroxysuccinimide) solution (1 mg·mL^{-1}) were added and kept shaking at 4 °C for 6 h. EDC and NHS can activate the carboxyl group and help HGC to be modified and immobilized on the surface of Cu_2O@PdAg. Excess coupling reagent and unbound HGC were removed by washing with PBS after cryogenic centrifugation. The resulting pellet was then redispersed in 1 mL of PBS. Then 0.5 mL of 1% BSA was added, and the mixture was shaken at 4 °C for 3 h. Unbound BSA was removed by centrifugation again with PBS. Finally, it was mixed with 1 mL of Ab_2 solution (1 μg·mL^{-1}) and shaken for 3 h. After centrifugation, it was dissolved in 2 mL of PBS to obtain a Cu_2O@PdAg-HGC-Ab_2 bioconjugate solution with a concentration of 1.5 mg·mL^{-1}.

Construction of quenching ECL immunosensor

The construction process of the immunosensor in this work is shown in Scheme 1. First, 10 μL of CdS@CeO_2-NH_2 solution with a concentration of 0.5 mg·mL^{-1} was dropped onto the surface of the polished and dried glassy carbon electrode. A uniform film was formed after air-drying at room temperature. Then 6 μL of HGC solution and Ab_1 solution (both 1 μg·mL^{-1}) were drop-coated on the electrode surface in turn and incubated in a 4 °C refrigerator. To block non-specific binding sites, 3 μL of 1% BSA was dropped on the electrode surface and incubated at 4 °C. A series of different concentrations of PSA (5 μL) were then coated on the electrodes to form a sandwich structure, which was incubated in a refrigerator at 4 °C for 2 h. Finally, 6 μL of Cu_2O@PdAg-HGC-Ab_2 solution (1.5 mg·mL^{-1}) was dripped on the electrode surface, and the construction of the immunosensor was completed.

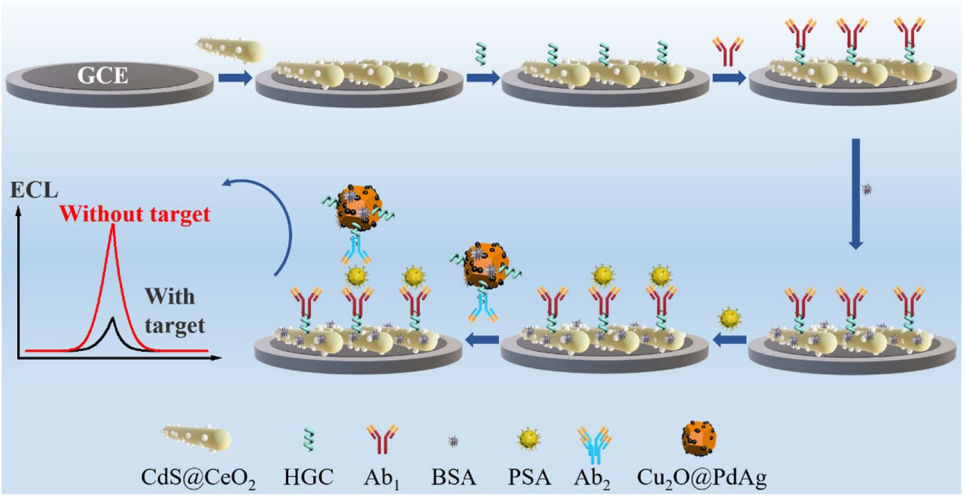

Scheme 1 Construction process of quenched ECL immunosensor

After each step of electrode modification, the electrode surface was rinsed with PBS to remove unsuccessfully loaded material.

Results and discussion

Characterization of nanocomposites

In this work, the morphologies of the synthesized materials were characterized by scanning electron microscopy (SEM) and transmission electron microscopy (TEM). As shown in Fig. 1A, CdS is a smooth and uniform rod-like structure with a cross-sectional diameter of about 10 nm. There are many obvious characteristic peaks in the XRD spectrum of CdS in Fig. 1E, such as 24.81°, 26.51°, 28.18°, 36.62°, 43.68°, 47.84°, 50.88°, 51.82°, 52.80°, and 66.77°, which can be corresponding to (100), (002), (101), (102) (110), (103), (200), (112), (201), and (203) crystallographic planes in the standard XRD spectrum (PDF#41–1049), demonstrating the successful synthesis of CdS. Figure 1B is the SEM image of the composite CdS@CeO_2. It can be seen that the surface is uneven, and the surface of the smooth CdS nanorods is uniformly loaded with a layer of fine CeO_2 particles. The specific surface area is significantly increased, which is conducive to the attachment of molecules such as antigens and antibodies. In addition, the XRD peak pattern of the CdS@CeO_2 composite (Fig. 1E) not only retains the original CdS diffraction peaks, but also has 8 more characteristic peaks (28.55°, 33.08°, 47.48°, 56.34°, 59.09°, 69.42°, 76.70°, 79.08°). It can correspond to the (110), (200), (220), (311), (222), (400), (331), and (420) plane in the standard XRD pattern of CeO_2 (PDF#43–1002). This indicates that CeO_2 nanoparticles are successfully loaded onto the surface of CdS nanorods without destroying the original crystal structure of CdS. UV–vis spectrum also proved the successful synthesis of CdS@CeO_2 (Fig. 2A).

It can be seen from Fig. 1C that Cu_2O is a regular tetrahedron structure with smooth surface composed of 6 regular quadrilaterals and 8 regular hexagons, with a side length of about 200 nm. The specific surface area is conducive to the loading of small particle size substances. As shown in Fig. 1F, the diffraction peaks at 29.55°, 36.42°, 42.30°, 61.34°, 73.53°, and 77.32° of the XRD pattern of Cu_2O are consistent with the crystal plane located at (110), (111), (200), (220), (311), and (222) in the standard spectrum (PDF#05–0667), which proves that the preparation of Cu_2O is successful. In Fig. 1D, PdAg is a smooth spherical structure with a diameter of about 100 nm, which is very easy to adhere or aggregate on the surface of large-scale structures due to its small size. Based on this, Cu_2O@PdAg composites with excellent properties were synthesized and characterized by UV–vis absorption spectra. In Fig. 2B, the UV–vis absorption intensity of PdAg nanospheres in the range of 200–400 nm is basically unchanged, and the absorption is gradually weakened in the range of 400–800 nm. The UV–vis absorption of Cu_2O increases gradually in the wavelength range of 200–800 nm, with a small absorption peak at 510 nm and a broad absorption peak at 565–745 nm. The composite Cu_2O@PdAg retains the absorption peak around 500 nm, and the peak at 565–745 nm has a large shift. The difference between the two curves indicates that the Cu_2O@PdAg composite was successfully prepared.

Quenching ECL mechanism

In order to get the best performance of the immunosensors, the conditions of c(CdS@CeO_2), c(Cu_2O@PdAg), c($K_2S_2O_8$), and pH were screened (Figure S1), and the best

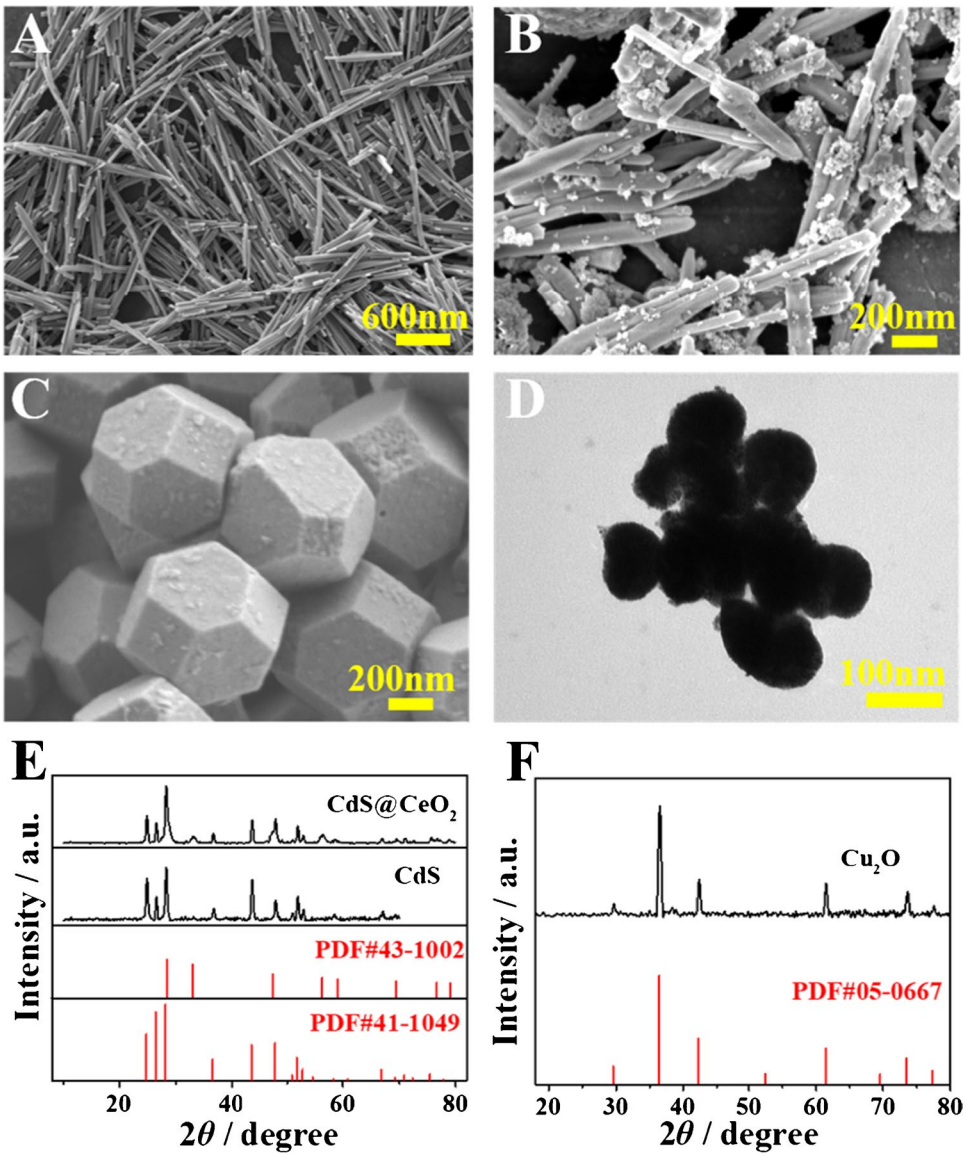

Fig. 1 SEM images of CdS nanorods (**A**), CdS@CeO_2 nanocomposites (**B**) and Cu_2O tetradecahedrons (**C**). (**D**) TEM images of PdAg nanospheres. (**E**) XRD patterns of CdS and CdS@CeO_2. (**F**) XRD pattern of Cu_2O tetradecahedron

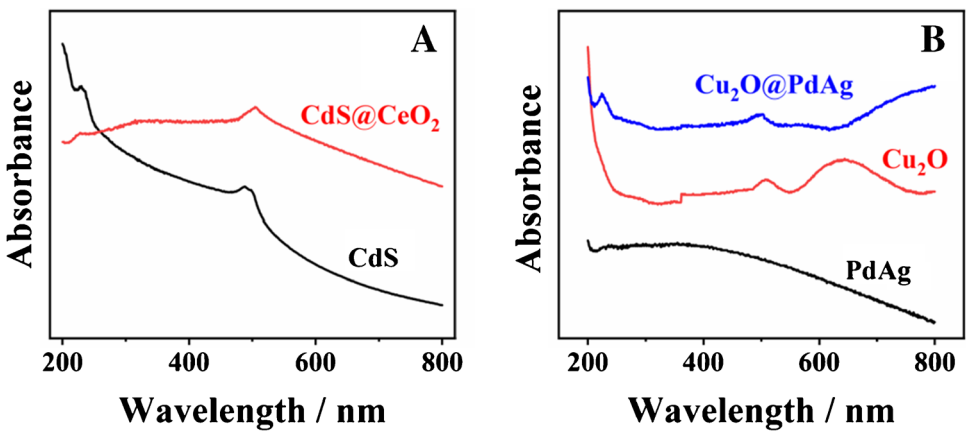

Fig. 2 (**A**) UV–vis absorption spectra of CdS and CdS@CeO_2. (**B**) UV–vis absorption spectra of Cu_2O, PdAg and Cu_2O@PdAg

operating environment was obtained (the following tests were all under the best conditions).

The possible ECL quenching mechanism of the immunosensor was discussed by ECL tests in different systems. It can be seen that independent $K_2S_2O_8$ can generate ECL signal, but the signal intensity was not high. After the electrode surface was modified with CdS@CeO_2, the ECL intensity of curve b was significantly enhanced, while the ECL intensity of curve c was almost zero. The above results indicate that CdS@CeO_2 requires the presence of the coreactant $K_2S_2O_8$ to achieve cathodic ECL luminescence, and cannot emit light alone. On this basis, after adding the quencher Cu_2O@PdAg, the ECL signal decreased significantly, which proves that Cu_2O@PdAg has a strong quenching effect on the CdS@CeO_2-$K_2S_2O_8$ system.

In order to further explore the quenching mechanism of Cu_2O@PdAg, the UV–vis absorption spectrum of Cu_2O@PdAg (curve a) and the ECL emission spectrum of CdS@CeO_2 (curve b) in Fig. 3B were compared. It can be observed that the luminophore CdS@CeO_2 has ECL emission in the wavelength range of 400–900 nm, a small emission peak at 516 nm, and a high and relatively broad emission peak at 780 nm, while Cu_2O@PdAg has strong UV–vis absorption in the same wavelength range of 400–900 nm, with a sharp absorption peak at 500 nm. After 625 nm, the UV–vis absorption gradually increases, which is in good agreement with the ECL emission spectrum of CdS@CeO_2, with a large area of spectral overlap. Resonance energy transfer occurs due to the spectral overlap between CdS@CeO_2 and Cu_2O@PdAg, where CdS@CeO_2 is the energy donor and Cu_2O@PdAg is the energy acceptor.

As shown in Fig. 3C, when the voltage is swept in the range of − 1.6–0 V, CdS@CeO_2 gets an electron on the electrode surface to generate CdS@$CeO_2^{\bullet-}$ (Eq. 2), and $S_2O_8^{2-}$ is reduced to $SO_4^{\bullet-}$ free radicals and SO_4^{2-} (Eq. 1). The strongly oxidizing $SO_4^{\bullet-}$ reacts with CdS@$CeO_2^{\bullet-}$ to obtain the excited state of CdS@CeO_2 (CdS@CeO_2^{*}). And when CdS@CeO_2^{*} transitions back to the ground state, an ECL signal is generated (Eqs. 3–4). Based on the principle of resonance energy transfer (ECL-RET), Cu_2O@PdAg has a quenching effect on the ECL signal of CdS@CeO_2.

$$S_2O_8^{2-} + e^- \rightarrow SO_4^{\bullet-} + SO_4^{2-} \quad (1)$$

$$CdS@CeO_2 + e^- \rightarrow CdS@CeO_2^{\bullet-} \quad (2)$$

$$CdS@CeO_2^{\bullet-} + SO_4^{\bullet-} \rightarrow CdS@CeO_2^{*} + SO_4^{2-} \quad (3)$$

$$CdS@CeO_2^{*} \rightarrow CdS@CeO_2 + h\nu \quad (4)$$

Performance testing for PSA

In order to realize the sensitive detection of PSA by the immunosensor, the ECL signals of a series of different

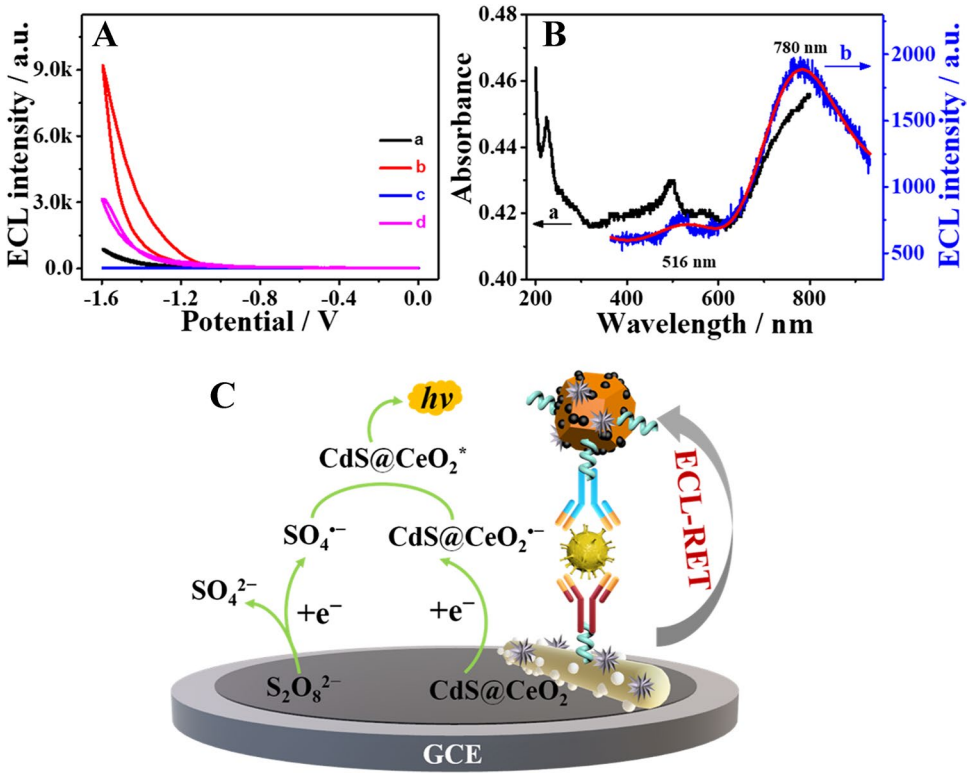

Fig. 3 (**A**) ECL responses under different conditions: (a) GCE, (b) CdS@CeO_2/GCE, (d) Cu_2O@PdAg/CdS@CeO_2/GCE in PBS (pH 7.4) containing 150 mM $K_2S_2O_8$, (c) CdS@CeO_2/GCE in PBS (pH 7.4) without $K_2S_2O_8$. (**B**) UV–vis absorption spectrum of Cu_2O@PdAg (curve a) and ECL emission spectrum of CdS@CeO_2 (curve b). (**C**) Detailed luminescence process of CdS@CeO_2- $K_2S_2O_8$ system in the presence of Cu_2O@PdAg

concentrations of PSA were tested under optimal conditions. In Fig. 4A, the ECL signal intensity decreased with increasing PSA concentration, and the ECL-time curves at each concentration were shown in Fig. 4B. Through linear regression calculation, it was found that when the PSA concentration was in the range of 10 fg·mL^{-1}–100 ng·mL^{-1}, the ECL intensity was inversely proportional to the logarithm of the PSA concentration. The linear equation was $I = -909.31 \lg c + 5187.8$, and the correlation coefficient was 0.984. The detection limit was 5.6 fg·mL^{-1} (S/N = 3). Compared with other literatures on PSA detection (Table 1), it can be found that the immunosensor has a wide detection range and extremely low detection limit, showing great potential and development value for sensitive detection of prostate cancer.

Stability, selectivity, and repeatability of immunosensors

The performance of the immunosensor plays a decisive role in the detection. As shown in Fig. 5A, the ECL signal is very stable over multiple consecutive voltage sweeps, with a relative standard deviation (RSD) of only 0.73%. In addition, the immunosensor has excellent storage stability. Although the ECL intensity after being placed in a 4 °C refrigerator for 25 days is slightly reduced, it can still reach 89.7% of the ECL intensity before storage, which does not affect the relevant detection results. To test the selectivity of the immunosensor, neuron-specific enolase (NSE), insulin (Ins), carcinoembryonic antigen (CEA), and aflatoxin (AFT) were used as interferers, including hormones, proteins, and other antigens that may interfere with the results. In Fig. 5C, electrode a is a blank sample. And electrodes b–e are loaded with 10 ng·mL^{-1} of different interfering substances, respectively. It can be found that the obtained ECL intensity is higher. After loading with PSA (1 ng·mL^{-1}), the ECL signal of the f electrode was significantly reduced. The hybrid included PSA at 1 ng·mL^{-1} and the rest of the interfering species at 10 ng·mL^{-1}, and its ECL signal did not change much compared to the electrode f. It shows that the immunosensor has good selectivity and is less affected by the interference of other substances. Under the same test conditions, the ECL signals of multiple different electrodes were almost identical, and the RSD was only 0.43%, confirming the excellent reproducibility of the constructed immunosensor (Fig. 5D).

As shown in Figure S2A, the CV curve (curve a) of the bare glassy carbon electrode (GCE) has obvious symmetrical redox peaks. Since the emitter CdS@CeO_2 is a semiconductor, the electron transfer rate is slowed down and the current peak is significantly reduced (curve b). Due to the non-conductivity of biological protein molecules, the current peaks decreased layer by layer after continuing to modify HGC, Ab_1, BSA, PSA, and Ab_2 bioconjugates

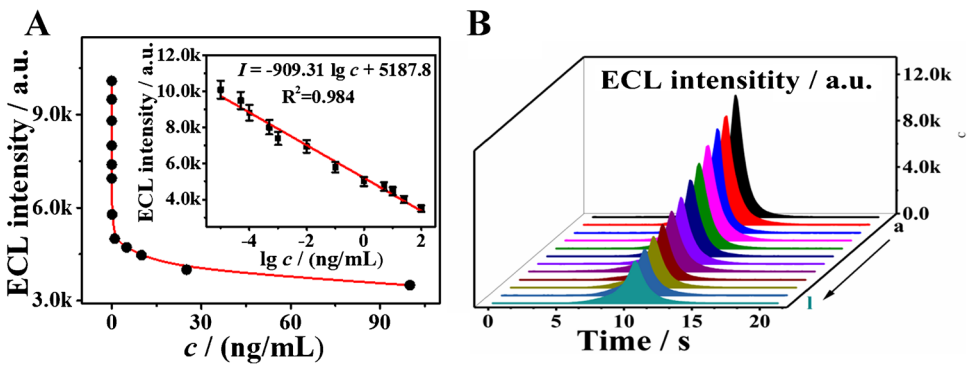

Fig. 4 ECL response at different PSA concentrations, insets are calibration working curve (**A**) and (**B**) the ECL intensity-time curves of different concentrations of NSE detected by immunosensor: (a) 0.00001, (b) 0.00005, (c) 0.0001, (d) 0.0005, (e) 0.001, (f) 0.01, (g) 0.1, (h) 1, (i) 5, (j) 10, (k) 25, (l) 100 ng·mL.$^{-1}$. The error bars show the standard deviation of quintuplicate tests ($N = 5$)

Table 1 Performance comparison with other literature on detection of PSA

Methods	Materials	Linear range (ng·mL^{-1})	Detection limit (pg·mL^{-1})	Reference
Photoelectrochemistry	$CdTe/TiO_2$	0.005–20	1.5	[28]
Electrochemistry	Fe_3O_4@COF	0.0001–10	0.03	[29]
Fluoroimmunoassay	Ag@SiO_2@SiO_2-RuBpy	0.1–100	27	[30]
Electrochemiluminescence	GSH-AGIS	0.00005–1	0.01	[31]
Electrochemiluminescence	Fe_3O_4 NP@lipid/Ru1/Chol-peptide-Fc	0.01–1	3	[32]
Electrochemiluminescence	CdS@CeO_2	0.00001–100	0.0056	This work

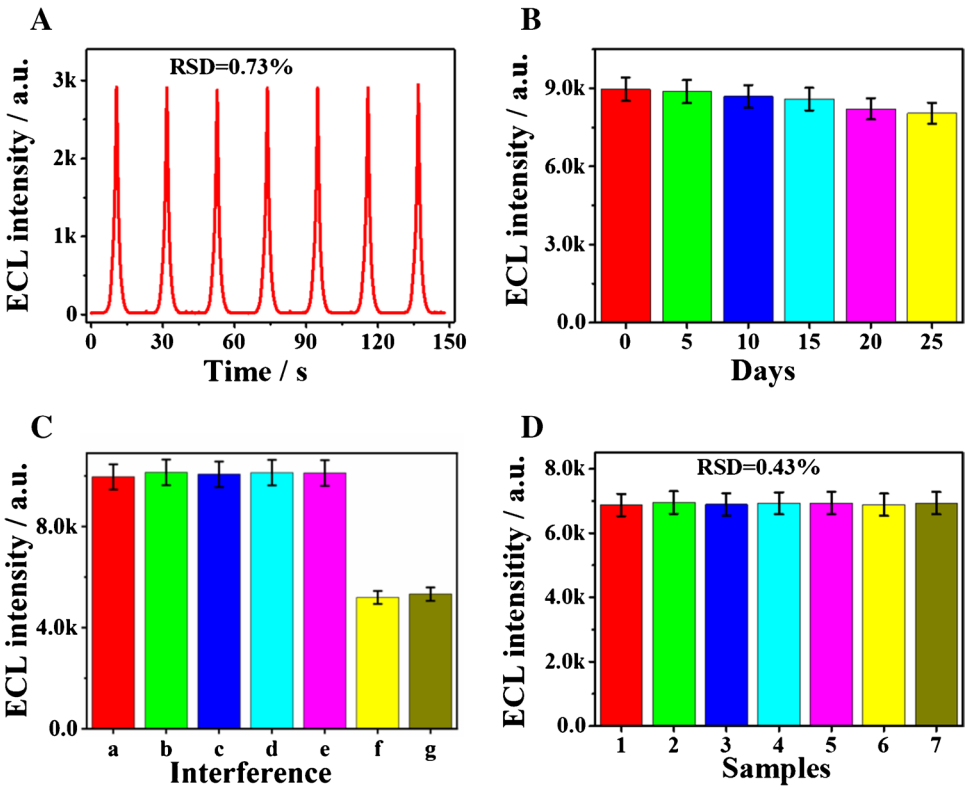

Fig. 5 (**A**) The stability of the immunosensor under continuous cyclic potential scans for 7 cycles. (**B**) The storage stability of the immunosensor. (**C**) The selectivity of the immunosensor under different interference conditions: (a) blank, (b) NSE, (c) Ins, (d) CEA, (e) AFT, (f) PSA, (g) hybrid. (**D**) Repeatability of seven different electrodes. The error bars show the standard deviation of quintuplicate tests ($N=5$)

(curves c–g). The resistance of GCE in Figure S2B is very small, and the resistance increases continuously during the layer-by-layer modification, which can correspond to the decrease of the current peak value in the CV curve. The above results fully demonstrate that the construction of the immunosensor is successful.

PSA sample testing

In order to verify the practical performance of the immunosensor, the sample recovery test of PSA in human serum samples was carried out by the spike recovery method. The results are shown in Table 2, the recoveries were 99.8–101%, and the relative standard deviation (RSD) was 0.85–1.6%, which proved that the immunosensor has good accuracy and sensitivity, and can be applied to the detection of PSA concentration in samples. In addition, an enzyme-linked immunoassay (ELISA) kit was used to compare with this method. The standard concentration of PSA provided in the ELISA kit was diluted to obtain a test sample with a concentration of 2.77 ng·mL^{-1}. It can be concluded from Table 3 that there is no significant difference between the constructed immunosensor and the detection results obtained by the ELISA kit. The accuracy and practicability of the immunosensor in detection are proved by the comparison of F values.

Conclusion

In this work, a quenching immunosensor for sensitive detection of PSA was constructed based on the resonance energy transfer between CdS@CeO_2 and Cu_2O@PdAg. CeO_2 particles are loaded onto the surface of CdS nanorods to form a CdS@CeO_2 heterostructure, which reduces the toxicity of CdS and enhances the overall biocompatibility, thereby

Table 2 Application of the immunosensor in serum sample analysis

Sample (ng·mL^{-1})	Added (ng·mL^{-1})	Detected (ng·mL^{-1})	Average (ng·mL^{-1})	RSD (%)	Recovery (%)
2.32	1.05	3.39, 3.34, 3.41, 3.35, 3.38	3.37	0.85	100.0
	2.68	5.12, 4.92, 4.99, 5.07, 4.98	5.02	1.6	100.7
	5.09	7.48, 7.29, 7.36, 7.39, 7.49	7.40	1.1	99.8

Table 3 Comparison of this method and ELISA kit for the analysis of human serum samples

Method	Sample ($ng \cdot mL^{-1}$)	Detected ($ng \cdot mL^{-1}$)	Average ($ng \cdot mL^{-1}$)	*s*	RSD (%)	Relative error (%)	F^a value
ELISA	2.77	2.72, 2.79, 2.75, 2.73, 2.79	2.76	0.033	1.2	−0.72	1.65
This work	2.77	2.76, 2.73, 2.81, 2.71, 2.71	2.74	0.042	1.5		

[a]The *F* values refer to comparison of the proposed method with ELISA kit. The theoretical values at 95% confidence limits: $F = 6.39$, $F = \frac{S^2_{max}}{S^2_{min}}$

realizing the detection of biomolecules. Cu_2O has a regular tetradecahedral structure with a large specific surface area and a large light absorption coefficient, which can effectively quench the cathode ECL signal of CdS@CeO_2. In addition, the bimetallic PdAg nanospheres are loaded on the surface of Cu_2O, which can better connect with proteins such as antigens and antibodies, and improve the conduction rate and the sensitivity of the immunosensor. The final constructed immunosensor realizes ultra-low concentration detection of PSA. CdS is an excellent ECL emitter, but its application is limited by its biological toxicity. It is a challenge to find other ways to reduce its biological toxicity.

Supplementary Information The online version contains supplementary material available at https://doi.org/10.1007/s00604-023-05635-z.

Funding This research was financially supported by the Innovation Team Project of Colleges and Universities in Jinan (No. 2019GXRC027), the National Natural Science Foundation of China (Nos. 22274063, 51904114, 21777056, 21675063), and the Special Foundation for Taishan Scholar Professorship of Shandong Province.

Declarations

Conflict of interest The authors declare no competing interests.

References

1. Numan A, Singh S, Zhan Y, Li L, Khalid M, Rilla K, Ranjan S, Cinti S (2022) Advanced nanoengineered-customized point-of-care tools for prostate-specific antigen. Mikrochim Acta 189:27. https://doi.org/10.1007/s00604-021-05127-y
2. Usman A (2022) Nanoparticle enhanced optical biosensing technologies for prostate specific antigen biomarker detection. IEEE Rev Biomed Eng 15:122–137. https://doi.org/10.1109/Rbme.2020.3035273
3. Merriel SWD, Pocock L, Gilbert E, Creavin S, Walter FM, Spencer A, Hamilton W (2022) Systematic review and meta-analysis of the diagnostic accuracy of prostate-specific antigen (PSA) for the detection of prostate cancer in symptomatic patients. BMC Med 20:54. https://doi.org/10.1186/s12916-021-02230-y
4. Liu PK, Meng H, Zhang G, Song L, Han Q, Wang C, Fu YZ (2021) Ultrasensitive dual-quenching electrochemiluminescence immunosensor for prostate specific antigen detection based on graphitic carbon nitride quantum dots as an emitter. Mikrochim Acta 188:350. https://doi.org/10.1007/s00604-021-05015-5
5. Balk SP, Ko YJ, Bubley GJ (2003) Biology of prostate-specific antigen. J Clin Oncol 21:383–391. https://doi.org/10.1200/JCO.2003.02.083
6. Song L, Wu JL, Zhang G, Liu PK, Kuang GR, Fu YZ (2021) Novel gold nanoparticles functionalized Mo-polydopamine hollow sphere as an efficient quencher in conjugated microporous polymer electrochemiluminescent system. Sens Actuators B Chem 344:130130. https://doi.org/10.1016/j.snb.2021.130130
7. Ahmed HA, Azzazy HME (2013) Power-free chip enzyme immunoassay for detection of prostate specific antigen (PSA) in serum. Biosens Bioelectron 49:478–484. https://doi.org/10.1016/j.bios.2013.05.058
8. Zhang LJ, Luo ZB, Zeng RJ, Zhou Q, Tang DP (2019) All-solid-state metal-mediated Z-scheme photoelectrochemical immunoassay with enhanced photoexcited charge-separation for monitoring of prostate-specific antigen. Biosens Bioelectron 134:1–7. https://doi.org/10.1016/j.bios.2019.03.052
9. Zhao YT, Gao W, Ge XX, Li SQ, Du D, Yang HP (2019) CdTe@SiO_2 signal reporters-based fluorescent immunosensor for quantitative detection of prostate specific antigen. Anal Chim Acta 1057:44–50. https://doi.org/10.1016/j.aca.2019.01.019
10. Zhou ZM, Feng Z, Zhou J, Fang BY, Qi XX, Ma ZY, Liu B, Zhao YD, Hu XB (2015) Capillary electrophoresis-chemiluminescence detection for carcino-embryonic antigen based on aptamer/graphene oxide structure. Biosens Bioelectron 64:493–498. https://doi.org/10.1016/j.bios.2014.09.050
11. Feng SY, Zheng ZC, Xu YJ, Lin JY, Chen GN, Weng CC, Lin D, Qiu SF, Cheng M, Huang ZF, Wang L, Chen R, Xie SS, Zeng HS (2017) A noninvasive cancer detection strategy based on gold nanoparticle surface-enhanced Raman spectroscopy of urinary modified nucleosides isolated by affinity chromatography. Biosens Bioelectron 91:616–622. https://doi.org/10.1016/j.bios.2017.01.006
12. Dai L, Li YY, Wang YG, Luo XL, Wei D, Feng R, Yan T, Ren X, Du B, Wei Q (2019) A prostate-specific antigen electrochemical immunosensor based on Pd NPs functionalized electroactive Co-MOF signal amplification strategy. Biosens Bioelectron 132:97–104. https://doi.org/10.1016/j.bios.2019.02.055
13. Chen MM, Xu CH, Zhao W, Chen HY, Xu JJ (2022) Single cell imaging of electrochemiluminescence-driven photodynamic therapy. Angew Chem Int Edit 61:e202117401. https://doi.org/10.1002/anie.202117401
14. Xiao SY, Wang XY, Yang CP, Jiang YJ, Zhen SJ, Huang CZ, Li YF (2022) Electrochemiluminescence resonance energy transfer system based on silver metal–organic frameworks as a double-amplified emitter for sensitive detection of miRNA-107. Anal Chem 94:1178–1186. https://doi.org/10.1021/acs.analchem.1c04368
15. Ma XM, Kang Q, Li MM, Fu L, Zou GZ, Shen DZ (2022) Sensitive, signal-modulation strategy for discrimination of ECL spectra and investigation of mutual interactions of emitters. Anal Chem 94:3637–3644. https://doi.org/10.1021/acs.analchem.1c05217
16. Tu TT, Sun Y, Lei YM, Chai YQ, Zhuo Y, Yuan R (2022) Pyrenecarboxaldehyde encapsulated porous TiO_2 nanoreactors for monitoring cellular GSH levels. Nanoscale 14:5751–5757. https://doi.org/10.1039/d2nr00784c
17. Zhang JL, Yao LY, Yang Y, Liang WB, Yuan R, Xiao DR (2022) Conductive covalent organic frameworks with conductivity- and pre-reduction-enhanced electrochemiluminescence for

ultrasensitive biosensor construction. Anal Chem 94:3685–3692. https://doi.org/10.1021/acs.analchem.1c05436
18. Lu HJ, Xu JJ, Zhou H, Chen HY (2020) Recent advances in electrochemiluminescence resonance energy transfer for bioanalysis: fundamentals and applications. Trends Anal Chem 122:115746. https://doi.org/10.1016/j.trac.2019.115746
19. Chen C, Hildebrandt N (2020) Resonance energy transfer to gold nanoparticles: NSET defeats FRET. Trends Anal Chem 123:115748. https://doi.org/10.1016/j.trac.2019.115748
20. Jeong D, Jo W, Jeong J, Kim T, Han S, Son MK, Jung H (2022) Characterization of Cu_2O/CuO heterostructure photocathode by tailoring CuO thickness for photoelectrochemical water splitting. RSC Adv 12:2632–2640. https://doi.org/10.1039/d1ra08863g
21. Sundarapandi M, Shanmugam S, Ramaraj R (2022) Tuning Cu_2O shell on gold nanocube core employing amine-functionalized silane for electrocatalytic nitrite detection. ACS Appl Nano Mater 5:1674–1682. https://doi.org/10.1021/acsanm.1c04459
22. Xing B, Zhang T, Han Q, Wei Q, Wu D (2019) Electrochemiluminescent immunoassay for insulin by using a quencher pair consisting of CdS: Eu nanoclusters loaded with multiwalled carbon nanotubes on reduced graphene oxide nanoribbons and gold nanoparticle-loaded octahedral Cu2O. Microchim Acta 186:500. https://doi.org/10.1007/s00604-019-3640-1
23. Oh JW, Takaloo AV, Baek SD, Myoung JM (2022) Efficient electrochemiluminescence devices using Pd nanoparticle-anchored TiO_2 nanorod electrodes with high catalytic activity. Appl Surf Sci 586:152864. https://doi.org/10.1016/j.apsusc.2022.152864
24. Liu SH, Jia Y, Xue JW, Li YW, Wu ZL, Ren X, Ma H, Li Y, Wei Q (2020) Bifunctional peptide-biomineralized gold nanoclusters as electrochemiluminescence probe for optimizing sensing interface. Sens Actuators B Chem 318:128278. https://doi.org/10.1016/j.snb.2020.128278
25. Yang L, Fan DW, Zhang Y, Ding CF, Wu D, Wei Q, Ju HX (2019) Ferritin-based electrochemiluminescence nanosurface energy transfer system for procalcitonin detection using HWRGWVC heptapeptide for site-oriented antibody immobilization. Anal Chem 91:7145–7152. https://doi.org/10.1021/acs.analchem.9b00325
26. Song XZ, Zhao L, Luo CN, Ren X, Yang L, Wei Q (2021) Peptide-based biosensor with a luminescent copper-based metal–organic framework as an electrochemiluminescence emitter for trypsin assay. Anal Chem 93:9704–9710. https://doi.org/10.1021/acs.analchem.1c00850
27. Yang L, Jia Y, Wu D, Zhang Y, Ju HX, Du Y, Ma HM, Wei Q (2019) Synthesis and application of CeO_2/SnS_2 heterostructures as a highly efficient coreaction accelerator in the luminol–dissolved O_2 system for ultrasensitive biomarkers immunoassay. Anal Chem 91:14066–14073. https://doi.org/10.1021/acs.analchem.9b03796
28. Zhao JE, Wang SP, Zhang SB, Zhao PN, Wang JR, Yan M, Ge SG, Yu JH (2020) Peptide cleavage-mediated photoelectrochemical signal on-off via CuS electronic extinguisher for PSA detection. Biosens Bioelectron 150:111958. https://doi.org/10.1016/j.bios.2019.111958
29. Liang H, Xu HB, Zhao YT, Zheng J, Zhao H, Li GL, Li CP (2019) Ultrasensitive electrochemical sensor for prostate specific antigen detection with a phosphorene platform and magnetic covalent organic framework signal amplifier. Biosens Bioelectron 144:111691. https://doi.org/10.1016/j.bios.2019.111691
30. Xu DD, Deng YL, Li CY, Lin Y, Tang HW (2017) Metal-enhanced fluorescent dye-doped silica nanoparticles and magnetic separation: a sensitive platform for one-step fluorescence detection of prostate specific antigen. Biosens Bioelectron 87:881–887. https://doi.org/10.1016/j.bios.2016.09.034
31. Fu L, Fu KN, Gao XW, Dong ST, Zhang B, Fu SJ, Hsu H-Y, Zou GZ (2021) Enhanced near-infrared electrochemiluminescence from trinary Ag−In−S to multinary Ag−Ga−In−S nanocrystals via doping-in-growth and its immunosensing applications. Anal Chem 93:2160–2165. https://doi.org/10.1021/acs.analchem.0c03975
32. Yang XL, We YX, Wang ZM, Wang J, Qi HL, Gao Q, Zhang CX (2022) Highly efficient electrogenerated chemiluminescence quenching on lipid-coated multifunctional magnetic nanoparticles for the determination of proteases. Anal Chem 94:2305–2312. https://doi.org/10.1021/acs.analchem.1c05033